Title

Specific cation effects at aqueous solution−vapor interfaces: Surfactant-like behavior of Li+ revealed by experiments and simulations

Journal

Proceedings of the National Academy of Sciences of the United States of America, 114(51)

ISSN

0027-8424

Authors

Perrine, Kathryn A
Parry, Krista M
Stern, Abraham C
et al.

Publication Date

2017-12-19

DOI

10.1073/pnas.1707540114

Peer reviewed

Specific cation effects at aqueous solution–vapor interfaces: Surfactant-like behavior of Li^+ revealed by experiments and simulations

Kathryn A. Perrine[a,1], Krista M. Parry[a,1], Abraham C. Stern[a], Marijke H. C. Van Spyk[a], Michael J. Makowski[a], J. Alfredo Freites[a], Bernd Winter[b], Douglas J. Tobias[a,2], and John C. Hemminger[a,2]

[a]Department of Chemistry, University of California, Irvine, CA 92697-2025; and [b]Department of Molecular Physics, Fritz-Haber-Institut der Max-Planck-Gesellschaft, 14195 Berlin, Germany

Edited by Michael L. Klein, Temple University, Philadelphia, PA, and approved August 31, 2017 (received for review May 5, 2017)

It is now well established by numerous experimental and computational studies that the adsorption propensities of inorganic anions conform to the Hofmeister series. The adsorption propensities of inorganic cations, such as the alkali metal cations, have received relatively little attention. Here we use a combination of liquid-jet X-ray photoelectron experiments and molecular dynamics simulations to investigate the behavior of K^+ and Li^+ ions near the interfaces of their aqueous solutions with halide ions. Both the experiments and the simulations show that Li^+ adsorbs to the aqueous solution–vapor interface, while K^+ does not. Thus, we provide experimental validation of the "surfactant-like" behavior of Li^+ predicted by previous simulation studies. Furthermore, we use our simulations to trace the difference in the adsorption of K^+ and Li^+ ions to a difference in the resilience of their hydration shells.

ion adsorption | air–water interface | specific ion effects | Hofmeister series | aqueous ionic solvation

Myriad chemical and biochemical processes that occur in aqueous salt solutions exhibit trends that depend systematically on the identities of the salt ions. These trends, which are commonly referred to as specific ion effects, generally follow the Hofmeister series, a ranking of the ability of salt ions to precipitate proteins that was developed by Franz Hofmeister (1) in the late 1800s. The Hofmeister series applies, however, to a wide range of other seemingly unrelated phenomena, such as colloidal stability, critical micelle concentrations, chromatographic selectivity, protein denaturation temperatures, and the interfacial properties of aqueous salt solutions (2, 3). Early attempts to explain the Hofmeister series relied on the notion that salt ions have a long-range effect on the structure of water, with ions on one side of the series acting as "structure makers" and ions on the other side as "structure breakers" (2, 4). However, more recently, several experimental and computational studies have questioned the role of long-range ordering/disordering effects (4–9), and have provided compelling evidence that ion-specific behavior at aqueous interfaces must be taken into consideration when attempting to explain Hofmeister effects (7, 10–13).

Specific anion effects on the interfacial properties of aqueous salt solutions, such as surface tensions and surface potentials, closely follow the Hofmeister series for anions (14). For example, surface tension increments (STIs; differences between the surface tension of a salt solution and that of neat water) of sodium salts at the same concentration decrease in the order: $SO_4^{2-} > Cl^- > Br^- > NO_3^- > I^-$ (15, 16). Molecular dynamics (MD) simulations have predicted that the propensity of anions to adsorb to the solution–vapor interface follows the Hofmeister series in reverse (7, 14, 17), and this prediction has largely been confirmed experimentally (14, 18–22). Moreover, MD simulations have shown that, with few exceptions [e.g., SO_4^{2-} in $(NH_4)_2SO_4$ (23)], anions adsorb more strongly to the solution–air interface than their counter cations, and, consequently, electrical double layers are formed near the interface, with the anions residing in or near the topmost layer of the solution, and the cations residing below the anions (14, 24, 25). Surface potentials (26), phase-sensitive vibrational sum frequency generation (PS-VSFG) spectra (22, 27, 28), and X-ray photoelectron spectroscopic (XPS) data (19, 29–32) are consistent with the double layer picture.

Compared with anion-specific effects, cation-specific effects at the solution–air interface are generally observed to be relatively weak. For example, the concentration dependence of the STIs of LiCl, NaCl, and KCl are very similar (33). In one of the few studies that directly determined cation-specific effects on ion distributions in the interfacial region, XPS spectra and MD simulations revealed that Na^+ approaches the solution–air interface more closely than Rb^+, and that the interfacial population of Cl^- is greater in NaCl vs. RbCl solutions (31). PS-VSFG measurements, which provide indirect information on interfacial ion distributions via surface electric fields inferred from the imaginary part of the nonlinear susceptibility, have provided evidence of cation-specific effects on the strength of the electric double layer at the solution–air interfaces of nitrate, sulfate, and halide salt solutions (22, 27, 28).

In almost all aqueous salt solutions of salts containing alkali metal cations, the cations are excluded from the topmost layer of the solution (14). It has been suggested, based on MD simulations (34–36), that Li^+ may be an exception. Presently, Li^+ is the only metal cation that has been observed in MD simulations to exhibit the "surfactant-like" behavior displayed by certain anions. However, this theoretical prediction has not been confirmed experimentally. Here we report liquid-jet XPS (LJ-XPS) measurements of the interfacial ion distributions in potassium and lithium halide solutions that provide direct experimental

Significance

Ion adsorption to the interfaces of aqueous salt solutions plays a key role in a wide variety of chemical and biochemical processes. For example, the adsorption of ions to the surface of aqueous aerosol particles in the atmosphere influences their reactivity to gas-phase oxidants. While the so-called chaotropic anions (e.g., I^-, SCN^-, and ClO_4^-) are known to have strong adsorption propensities, inorganic cations are generally regarded as being repelled from aqueous solution–air interfaces. Here we report a concerted experimental and computational study that reveals that Li^+ adsorbs to the interfaces of aqueous lithium halide solutions and, hence, is an exceptional cation.

Author contributions: D.J.T. and J.C.H. designed research; K.A.P., K.M.P., A.C.S., M.H.C.V.S., M.J.M., J.A.F., B.W., D.J.T., and J.C.H. performed research; K.A.P., K.M.P., A.C.S., M.H.C.V.S., M.J.M., J.A.F., B.W., D.J.T., and J.C.H. analyzed data; and K.A.P., K.M.P., B.W., D.J.T., and J.C.H. wrote the paper.

The authors declare no conflict of interest.

This article is a PNAS Direct Submission.

[1]K.A.P. and K.M.P. contributed equally to this work.

[2]To whom correspondence may be addressed. Email: dtobias@uci.edu or jchemmin@uci.edu.

This article contains supporting information online at www.pnas.org/lookup/suppl/doi:10.1073/pnas.1707540114/-/DCSupplemental.

evidence that, indeed, Li^+ adsorbs to the solution–air interface, while K^+ does not. We also report MD simulations that qualitatively reproduce the LJ-XPS results and provide molecular-level insights into the origin of the differences in the behavior of Li^+ and K^+ at the solution–air interface.

Results and Discussion

Depth-Dependent Cation/Water Oxygen Ratios from LJ-XPS Spectra. LJ-XPS signals originating from the I4d and K2p orbitals in 2.0 M KI, and I4d and Li1s orbitals in 2.0 M LiI, are shown in Fig. 1 *A–C* for both low (probing the surface) and high (probing the bulk) photoelectron kinetic energy (KE). Comparison of the low (200 eV) and high (600 eV) KE spectra reveals that the I^- signal is greater at low KE than at high KE for both the KI (Fig. 1*A*) and LiI (Fig. 1*C*) solutions, consistent with the now well-established notion that the population of I^- ions is greater at the surface vs. the bulk in alkali iodide solutions (14, 19, 25). The K^+ signal is lower at low KE than at high KE (Fig. 1*B*), indicating a depletion of K^+ ions at the surface relative to the bulk of the KI solution, which is also consonant with the prevailing picture of ion distributions near the surfaces of aqueous alkali halide solutions (14, 25). In contrast, the Li^+ signal at low KE is significantly higher than that at high KE (Fig. 1*C*). Thus, the spectra in Fig. 1*C* and the integrated area ratios in Fig. 1*D* provide direct experimental confirmation of the prediction, made on the basis of MD simulations (34–36), that Li^+ ions adsorb to the aqueous solution-air interface.

The integrated area under each spectral curve in Fig. 1 *A–C* provides a measure of the concentration of each ion at a particular probe depth of the experiment. To this end, the spectral peaks are first normalized by their respective photoionization cross-section, photon flux, detection angle, and the electron transmission of the analyzer, as described in detail in *Materials and Methods* (29, 37, 38). To obtain ion concentrations, the normalized ion spectral peak areas are divided by the normalized water O1s peak area at the same photoelectron KE. Fig. 1*D* compares the ratio of normalized cation/O1s signals from 2.0 M KI and LiI solutions as a function of photoelectron KE (electron volts) or experimental probe depth. The experimental probe depth is a function of the attenuation of the photoelectrons as they escape from the solution. We plot our data (Fig. 1*D*) as a function of photoelectron kinetic energy, with the realization that the probe depth increases with photoelectron kinetic energy. The quantification of the probe depth is a subject of some debate, but a reasonable estimate for these aqueous solutions is that it is <10 Å at a KE of 200 eV, and >20 Å at KE of 600 eV to 800 eV (39).

The cation to oxygen ratios in the bulk (photoelectron KE ≥ 600 eV) of both KI and LiI solutions approximately exhibit the bulk stoichiometry within experimental statistics, thus validating our approach for obtaining depth profile information using LJ-XPS. To be more accurate, for the 2.0 M concentrations, the expected ratio would be 2:55.5 = 0.036, but this does not account for the water density change upon making the solution. We estimate this effect from the atomic radii of I^- (2.25 Å), Li^+ (0.71 Å), and K^+ (1.41 Å) (40), and from the van der Waals radius of water (1.6 Å), which yields slightly larger predicted bulk ratios, 0.039 for Li^+ and 0.040 for K^+. Uncertainties in the ionization cross-sections and the photon flux likely result in the difference between our measurements and the expected bulk ratios. We also point out that the signal intensities represent exponentially weighted electron contributions from different distances from the surface (29). Thus, there will be signal from the topmost layer, even for the largest KE of 800 eV measured here.

While the K2p/O1s ratio remains essentially constant at all depths probed, the Li1s/O1s ratio exceeds the bulk stoichiometric ratio in the interfacial region (photoelectron KE ≤ 400 eV) and increases as the probing depth (photoelectron KE) decreases. Thus, the data in Fig. 1*D* clearly show that the concentration of Li^+ ions near the surface of a 2.0 M LiI solution is greater than in the bulk, i.e., that Li^+ is displaying surfactant-like behavior.

The cation to water oxygen ratios shown in Fig. 1*D* as a function of photoelectron KE for 2.0 M KI and LiI solutions are compared with the corresponding results for other 2.0 M K^+ and Li^+ halide salt solutions (KCl, KBr, LiCl, and LiBr) in *SI Appendix*, Fig. S1 *A* and *B*. In all cases, the K2p/O1s ratios are essentially constant at all depths probed (200 eV to 800 eV) (*SI Appendix*, Fig. S1*A*). As in the case of LiI (Fig. 1*D*), the Li1s/O1s ratios also increase with decreasing probe depth in LiCl and LiBr (*SI Appendix*, Fig. S1*B*). At the lowest photoelectron KEs considered, the Li1s/O1s ratio increases in the order LiCl < LiBr < LiI. Thus, the extent of Li^+ adsorption tracks the reverse Hofmeister ordering of anion adsorption ($Cl^- < Br^- < I^-$) observed in previous XPS experiments (19) and MD simulations (24), as well as the new anion/O1s ratios measured as a function of photoelectron KE reported in *SI Appendix*, Fig. S1 *C* and *D*.

Depth-Dependent Anion/Cation Ratios from LJ-XPS Spectra. Anion/cation ratios were determined from the XPS spectra by following the same procedure used to obtain the cation/O1s ratios. The I4d/K2p and I4d/Li1s ratios in the 2.0 M KI and 2.0 M LiI

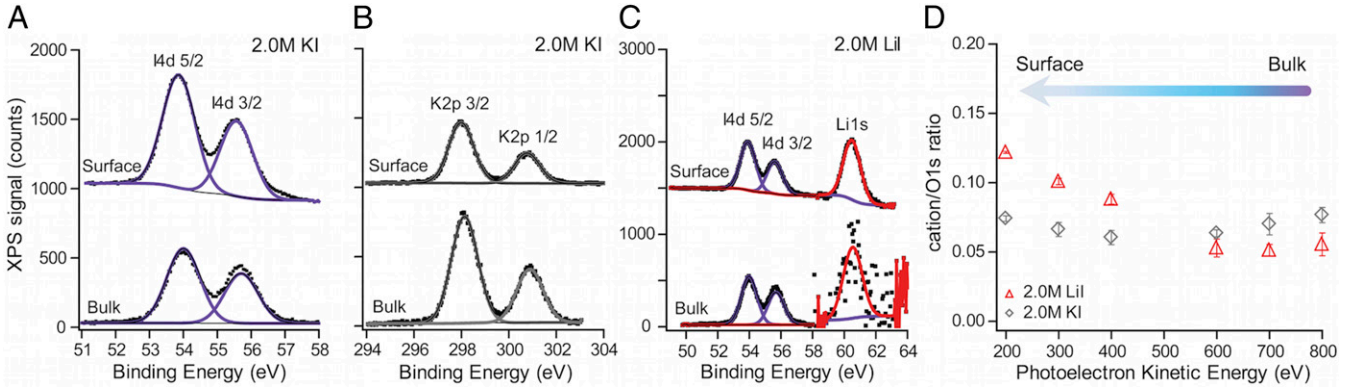

Fig. 1. Surface (200 eV KE) and bulk (600 eV KE) LJ-XPS spectra for (*A* and *B*) 2.0 M KI solutions and (*C*) LiI solutions. (*D*) Ratios of normalized cation/O1s signals plotted vs. photoelectron KE (probe depth). The zero of the vertical axis for the surface spectra in *A–C* has been offset to clearly display the surface and bulk spectra on the same plots. The spectral intensities in *A–C* have been corrected for the photon flux, and the photoionization cross-section so that direct comparisons of the intensities in these plots are meaningful. Since the I4d and the Li1s peaks occur in the same range of binding energies, the change in the scaling due to the significant difference in cross-sections is shown clearly (e.g., in *C*) by the discontinuity in the signal-to-noise as one goes from the I4d region to the Li1s region of the spectrum. The error bars shown in *D* include statistical errors in the determination of peak areas from the fitting routine and the precision of multiple experiments.

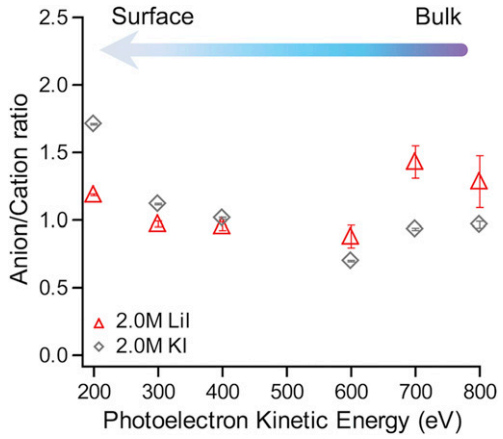

Fig. 2. Ratios of normalized XPS signals (I4d/K2p for KI and I4d/Li1s for LiI) plotted vs. photoelectron KE (probe depth) for 2.0 M KI and 2.0 M LiI solutions. The error bars include contributions from the statistics of the spectral fit to obtain peak areas and the precision of replicated experiments. The error bars do not include any contribution from the unknown uncertainty in the ionization cross-sections.

solutions, respectively, are plotted vs. photoelectron KE (probing depth) in Fig. 2. The I^-/K^+ ratio is greater than unity at the lowest photoelectron KE (200 eV) measured, indicating an excess of I^- anions over K^+ cations near the surface of the KI solution. This result is qualitatively consistent with previous XPS measurements (19), but the surface I^-/K^+ ratio in the present study is lower, presumably, in part, because the previous measurements were carried out on a deliquesced solid (saturated solution), whereas the measurements reported herein were carried out on a 2.0 M solution. The I^-/Li^+ ratio in 2.0 M LiI remains essentially constant near unity over the entire range of photoelectron KE (Fig. 2). This result is consistent with our observation that both the Li^+/water O (Fig. 1*D*) and I^-/water O (*SI Appendix*, Fig. S1*D*) ratios are greater, to roughly the same extent, at the solution surface than in the bulk. Thus, the anion/cation ratios confirm that Li^+ exhibits surfactant-like behavior, similar to I^-, while K^+ does not.

The LJ-XPS data reported in Figs. 1 and 2 were measured at a 20° angle between the polarization vector and the detection axis. To confirm that our findings are not affected by electron emission anisotropy, in a separate experiment, we measured the depth profile of 2.0 M LiI in comparison with 2.0 M NaI solutions at the magic angle (54.7°) where electron emission anisotropy is eliminated. In this case, only the orbital photoionization cross-sections are needed to obtain the ion concentration ratios (29, 38). The data measured at the magic angle for 2.0 M NaI and LiI solutions (*SI Appendix*, Fig. S2) confirm that the ion concentration ratios are independent of the experimental geometry. Given that the results are independent of the scattering angle, we collected the most complete set of data at a 20° scattering angle, where the signals are stronger.

Anion/cation ratios for 2.0 M KCl, KBr, and KI solutions are compared in *SI Appendix*, Fig. S3*A*, and those for 2.0 M LiCl, LiBr, and LiI solutions are compared in *SI Appendix*, Fig. S3*B*. The anion/K^+ ratio at the lowest photoelectron KE measured decreases in the order KI > KBr ≈ KCl (*SI Appendix*, Fig. S3*A*). The anion/Li^+ ratios at the lowest photoelectron KE are slightly less than one for the LiCl and LiBr solutions (*SI Appendix*, Fig. S3*B*), indicating that Li^+ ions are present with the anions in the interfacial region of those solutions.

Density Profiles from MD Simulations. Density profiles for ions and water oxygen atoms, computed from MD simulations of ∼2 M KI and ∼2 M LiI solutions and divided by the corresponding bulk densities (ρ_0), are plotted in Fig. 3 vs. the distance from the instantaneous solution–air interface (i.e., depth into the solution). Referring the density profiles to the instantaneous interface (see *SI Appendix* for definition and method of calculation) reveals structure in the interfacial region that is obscured when mean density profiles are computed on a static grid (41, 42). The water density profiles in Fig. 3 each display two peaks, one at ∼2 Å and the other at ∼5 Å below the interface, and the iodide density profiles display sharp peaks on the inner side of the topmost water layer, followed by a depletion zone centered around 5 Å below the interface, in which the ion density is lower than in the bulk. To maintain the electroneutrality of the interfacial region, the density profiles of the cations also contain peaks corresponding to enhanced ion populations in the interfacial region vs. the bulk. Both the K^+ (in KI) and Li^+ (in LiI) density profiles indicate enhanced populations in the zone of I^- depletion below the interfacial peak in the I^- density profiles. In addition, the Li^+ density profile displays a more prominent peak that is coincident with I^- interfacial peak. Thus, the MD simulation of 2 M LiI recapitulates the surfactant-like behavior of Li^+ inferred from the LJ-XPS data (Figs. 1 and 2).

The anion density profiles for K^+ and Li^+ solutions of all three halides considered show signal corresponding to surface-adsorbed anions that decreases in the order $I^- > Br^- > Cl^-$ (*SI Appendix*, Fig. S4). As for K^+ in the KI solution, the K^+ density profiles from the KBr and KCl solutions do not contain peaks corresponding to surface-adsorbed K^+ ions (*SI Appendix*, Fig. S4 *A–C*). On the other hand, as in the case of Li^+ in LiI, the Li^+ density profiles from the LiBr and LiCl solutions display a peak (for LiBr) or shoulder (for LiCl) corresponding to surface-adsorbed cations (*SI Appendix*, Fig. S4 *D–F*). Thus, the surfactant-like behavior of Li^+

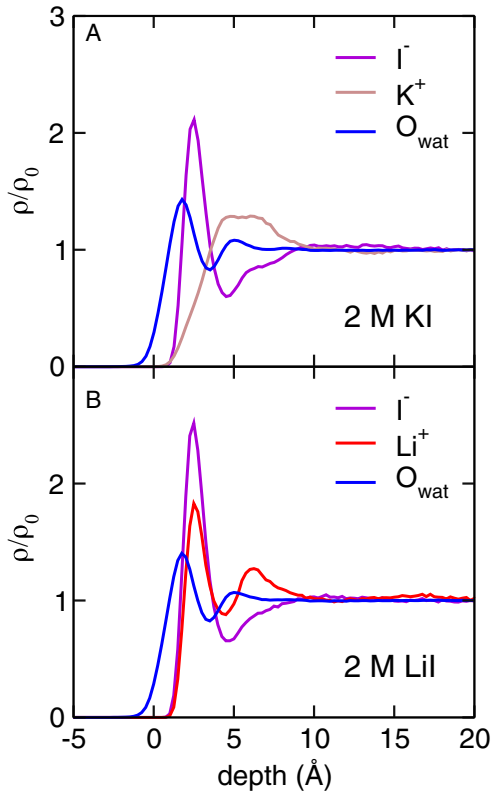

Fig. 3. Density profiles of ions and water oxygen atoms from MD simulations of (*A*) 2 M KI and (*B*) 2 M LiI solutions. The density profile of each species has been calculated with respect to the instantaneous solution–air interface and divided by the corresponding bulk density, ρ_0. The interface is located at depth = 0.

adsorption observed in the LiI solution is also seen in the LiBr and LiCl solutions, albeit to a lesser extent, and decreasing in the order LiI > LiBr > LiCl. The surface enhancement of Li^+ ions that we observed in lithium halide solutions agrees qualitatively with the results of previously reported MD simulations of 0.2 molal (m) and 1.0 m LiCl solutions (35), as well as an 8.6 m LiBr solution (36). We cannot quantitatively compare the extents of adsorption because of differences in the definition of the interface used to calculate density profiles.

Origins of the Different Interfacial Propensities of Li^+ and K^+ Ions. We can use our MD simulations to address the question of why Li^+ adsorbs to the topmost layer of water but K^+ does not. Although the relative importance of the various forces that drive ions toward or away from aqueous solution–air interfaces is a subject of ongoing inquiry (42–47), there is broad consensus that cavity formation promotes ion adsorption, and the loss of dispersion and local (hydration shell) electrostatic interactions accompanying ion desolvation opposes ion adsorption. In addition, when the simple point charge/extended (SPC/E) model is used for water molecules, as in the present study, there is an electrochemical surface potential, arising from broken symmetry in the water structure at ion–water and air–water interfaces, that favors the adsorption of anions and opposes the adsorption of cations (43, 44). In finite concentration solutions, such as those considered here, it is also possible that ion–ion interactions are different in bulk solution than in the interfacial region; in this case, there will be an additional electrostatic contribution to an ion's adsorption propensity.

The cavity term clearly does not contribute to the greater adsorption propensity of Li^+ vs. K^+, because K^+ is larger than Li^+. As we shall see in *Resilience of the Li^+ Solvation Shell*, Li^+ retains its full solvation shell even when it is in the topmost water layer, while K^+ sheds part of its solvation shell as it approaches the surface of the solution. Due to the loss of water molecules in the K^+ solvation shell, the concomitant loss of dispersion interactions opposes K^+ adsorption. On the other hand, since Li^+ retains its full solvation shell at the interface, the difference in dispersion interactions between Li^+ at the interface and in the bulk should be negligible. Thus, dispersion interactions are not expected to play an appreciable role in the adsorption of Li^+.

Next we examine the ion–ion and ion–water electrostatic interactions. The total electrostatic potential energy of K^+ ions in 2 M KI and Li^+ ions in 2 M LiI, as well as the contributions of cation–cation, cation–anion, and cation–water interactions, are plotted as functions of depth into the solutions in Fig. 4 *A* and *B*. Not surprisingly, the cation–cation electrostatic interaction energies are repulsive throughout each solution, and the shapes of the energy profiles resemble the shapes of the cation density profiles (Fig. 4 *C* and *D*). The cation–anion electrostatic interaction energies are attractive throughout each solution, and the cation–anion interaction energy profiles are practically mirror images of the cation–cation profiles. Thus, since these cation interactions mostly balance throughout the solution (*SI Appendix*, Fig. S5), the cation–ion electrostatic interactions do not contribute considerably to the adsorption propensity of either K^+ in 2 M KI or Li^+ in 2 M LiI.

The cation–water electrostatic interactions are attractive throughout each solution, and relatively very weak compared with the cation–cation and cation–anion electrostatic interactions (Fig. 4 *A* and *B*). For K^+ in the KI solution, there is a very shallow minimum in the cation–water electrostatic interaction energy profile (Fig. 4*A*), spanning roughly the same range of depth (~4 Å to 9 Å) as that of the enhanced K^+ density corresponding to the subsurface layer of K^+ ions (Fig. 4*C*). Upon moving closer to the interface, the K^+–water electrostatic energy rises to zero as the number of water molecules in the K^+ hydration shell drops from its bulk value of six (Fig. 4*E* and *SI Appendix*, Fig. S6*A*). Thus, desolvation constitutes a small penalty to the adsorption of K^+ ions to the solution surface. Likewise, the Li^+–water electrostatic interaction energy profile displays minima (Fig. 4*B*) where the Li^+ density profile contains maxima (Fig. 4*D*), with the deepest minimum coinciding with the surface layer of Li^+ ions. The Li^+ ion is able to maintain attractive Li^+–water interactions all of the way up to the solution surface because it retains its full hydration shell, consisting of four water molecules, throughout the solution (Fig. 4*F* and *SI Appendix*, Fig. S6*B*; see also ref. 34). The snapshot depicted in *SI Appendix*, Fig. S6*B* shows that the Li^+ ions that reside in the topmost layer of the solution can protrude from the solution surface.

More or less the same picture emerges from our MD simulations of potassium and lithium bromide and chloride solutions: In all cases, attractive cation–anion electrostatic interactions are essentially canceled by repulsive cation–cation electrostatic interactions throughout each solution (*SI Appendix*, Fig. S5). K^+ loses favorable electrostatic interactions with water due to desolvation as it approaches the solution surface (*SI Appendix*, Figs. S7 and S8). In the LiBr solution, Li^+ retains its solvation shell and favorable electrostatic interactions with water molecules in the topmost layer of solution (*SI Appendix*, Fig. S7). In the LiCl solution, Li^+ loses one water molecule from its solvation shell right at the surface (depth < 2 Å), but retains its full solvation shell and is slightly stabilized by cation–water interactions in the region of the maximum of the Li^+ density profile (*SI Appendix*, Fig. S8).

Resilience of the Li^+ Solvation Shell. The Li^+ solvation shell is remarkably resilient in a structural sense, i.e., Li^+ retains its coordination number of four, on average, throughout the LiCl, LiBr, and LiI solutions, except right at the surface (depth < 2 Å) of the LiCl solution. However, this structural resilience does not mean that water molecules do not move in and out of the Li^+ solvation shell, nor does it mean that the lifetime of a water molecule in the Li^+ solvation shell is the same throughout each solution. To quantify the lifetime of a water molecule in the Li^+ solvation shell, we have computed water residence times (see *SI Appendix* for definition and method of calculation) for Li^+ ions in the interfacial (depth < 5 Å) and bulk (depth > 5 Å) regions of the 2 M LiI solution. For comparison, we carried out the same calculations for K^+ ions in the 2 M KI solution, where the interfacial region was defined as depth < 10 Å. We obtained water residence times of 167 ps and 74 ps for Li^+ ions in the bulk and interfacial regions, respectively, of the LiI solution, and 11 ps and 9 ps for K^+ ions in the bulk and interfacial regions, respectively, of the KI solution. Thus, we find that water molecules have longer lifetimes in the cation solvation shell in the LiI solution than in the KI solution, and that the cation solvation shells are more dynamically labile/short-lived in the interfacial region compared with the bulk of both solutions.

Ion Pairing. The cation and anion density profiles overlap more in the topmost layer of the Li^+ solutions than in the K^+ solutions (Fig. 3 and *SI Appendix*, Fig. S4). The greater overlap in the Li^+ solutions raises the question: Is the extent of ion pairing correspondingly greater in the Li^+ solutions than in the K^+ solutions? To answer this question, we calculated the average number of ion pairs as a function of depth into the Li^+ and K^+ solutions. The results, plotted in *SI Appendix*, Fig. S9, show that the extent of ion pairing is actually greater in the K^+ solutions. Throughout each K^+ solution, except right at the surface (depth < 2 Å) of the KCl and KBr solutions where the K^+ density is negligible, K^+ is engaged in ~0.5 ion pairs (*SI Appendix*, Fig. S9). In contrast, in the Li^+ solutions, the average number of ion pairs throughout each solution is much lower (~0.07 in LiCl, ~0.01 in LiBr, and ~0.002 in LiI), except right at the surface (depth < 2 Å) of the LiCl solution.

Conclusions

We used a combination of LJ-XPS experiments and MD simulations to investigate specific cation effects at the aqueous

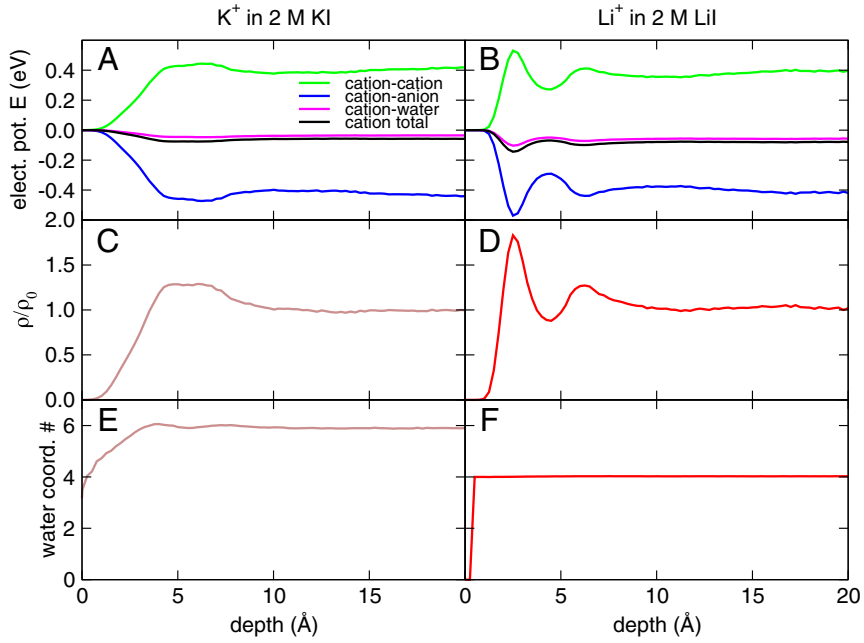

Fig. 4. Depth dependence of the electrostatic interaction energies of (*A*) K^+ ions in 2 M KI and (*B*) Li^+ ions in 2 M LiI. The green curves are contributions from cation–cation interactions, the blue curves are from cation–anion interactions, and the magenta curves are from cation–water interactions. The black curves are the total electrostatic interaction energies. (*C*) Density profile for K^+ ions in 2 M KI. (*D*) Density profile for Li^+ in 2 M LiI. (*E*) Number of water molecules in the first solvation shell of K^+ in 2 M KI. (*F*) Number of water molecules in the first solvation shell of Li^+ in 2 M LiI. All quantities in this figure were calculated with respect to the instantaneous solution–air interface. The interface is located at depth = 0.

solution–air interfaces of potassium and lithium halide solutions. The cation/oxygen and anion/cation ratios from the LJ-XPS experiments and the density profiles from the MD simulations show that Li^+ ions adsorb to the interface, but K^+ does not. Consistent with previous studies (14, 19, 25), both the LJ-XPS experiments and MD simulations also show that the iodide anion exhibits surfactant-like behavior. Moreover, the simulations predict that the halide anion adsorption propensity decreases in the order $I^- > Br^- > Cl^-$ in both K^+ and Li^+ solutions, and that the extent of anion adsorption does not depend significantly on the identity of the counter cation in the solutions considered here. The simulations provide evidence that the primary reason Li^+ ions are able to approach the interface more closely than K^+ is that Li^+ ions retain their full hydration shell, and the associated favorable ion–water electrostatic interactions, even in the topmost layer of the solution. In contrast, while K^+ ions retain their complete hydration shell up to the subsurface layer beneath the surface anion layer, as they approach the surface more closely, they shed part of their hydration shell and lose stabilizing electrostatic interactions with water molecules.

Materials and Methods

LJ-XPS Experiments. Liquid-jet experiments were performed at the Molecular Environmental Sciences beamline (11.0.2) at the Advanced Light Source (ALS) at Lawrence Berkeley National Laboratory (LBNL) (48–52). The details of the experimental setup and procedures have been described previously (21). Specific details of the experimental methods are provided in *SI Appendix*. In summary, a laminar flowing liquid microjet (Microliquids Inc.) of 21 μm diameter, held at 6 °C, in the presence of 1 Torr water vapor, was irradiated by X-rays from the synchrotron, resulting in the emission of photoelectrons. Photoelectrons were collected, energy analyzed, and detected via a four-stage differentially pumped lens and hemispherical analyzer system (Phoibos 150; Specs). Since the escape depth of the photoelectrons from the solution is strongly kinetic energy-dependent, the probe depth of the experiment can be adjusted by changing the X-ray photon energy, which sets the kinetic energy of the photoelectrons. Photoelectron KE between 200 eV (probing predominantly the interface) and 800 eV (probing the bulk of the liquid-jet solution) were used. The photoelectron spectra were normalized for atomic transition cross-sections (37), photon flux, analyzer transmission function, and transmission of the X-rays through the background water vapor, as decribed by Ottosson et al. (29). The X-ray transmission through water vapor was computed using the on-line program provided by the Center for X-ray Optics at LBNL (53). Salt solutions were prepared by weighing out each salt and dissolving with highly demineralized water (conductivity ∼0.2 μS/cm, 18.2 MΩ, deionized water), up to 100 mL. Salts were purchased, and included potassium iodide (>99.5%, puriss p.a; Sigma Aldrich), lithium iodide (99.9% trace metals basis; Sigma Aldrich), and sodium iodide (Sigma Aldrich).

MD Simulations. MD simulations of ∼2 M aqueous LiCl, LiBr, LiI, KCl, KBr, and KI solutions consisted of 1,728 water molecules and 68 ion pairs. The dimensions of the simulation cell were 30 Å × 30 Å × 140 Å for each system. Periodic boundary conditions were applied in all three dimensions, resulting in solution "slabs" ∼70 Å thick with two solution–vacuum interfaces at $z \approx \pm 35$ Å. The SPC/E model was used for water (54), and the ion force field parameters were taken from Horinek et al. (34) (see *SI Appendix*, Table S1 for a full listing of the force field parameters used in this study). The ion force fields we used were parameterized in conjunction with the SPC/E water model to reproduce the first peaks in the ion–water radial distribution functions, as well as ion solvation free energies and entropies (34). The resulting models were then used to calculate single-ion adsorption potentials of mean force, from which surface tensions were computed using an extended Poisson–Boltzmann theory (34). The resulting STIs, i.e., difference between the surface tension of a salt solution and the surface tension of neat water, agreed well with experimental measurements up to 1 M concentration (34). In *SI Appendix*, Table S2, we compare the STIs calculated from our MD simulations of ∼2 M lithium and potassium halide solutions with experimental data. Overall, the agreement is very good: The STIs are all positive and increase in the order MI < MBr < MCl, where M is K^+ or Li^+, and the STIs for the K^+ salts are mostly greater than those for the corresponding Li^+ salts.

The MD trajectories were generated using the Gromacs simulation suite (55) for 80 ns each with a timestep of 1 fs; the last 70 ns of each trajectory was used for analysis. The temperature was held constant at 300 K using a Berendsen thermostat (56) with velocity rescaling to ensure the correct kinetic energy distribution (57). Water molecules were held rigid using the SETTLE algorithm (58). The electrostatic energies and forces were calculated using the particle mesh Ewald method (59), and a cutoff of 9 Å was used to truncate the Lennard-Jones interactions and the real-space part of the Ewald sum.

ACKNOWLEDGMENTS. We are grateful to Hendrik Bluhm and Andrey Shavorskiy for discussions and assistance with the beam line and end-station. This work was supported by the National Science Foundation Grant CHE-0909227 and the Atmospheric Integrated Research at University of California, Irvine (AirUCI) Organized Research Unit. The experiments were carried out at the ALS beam line 11.0.2. The ALS is supported by the Director, Office of Science, Office of Basic Energy Sciences, of the US Department of Energy under Contract DE-AC02-05CH11231. B.W. acknowledges support from the Deutsche Forschungsgemeinschaft through the Collaborative Research Center 1109.

1. Hofmeister F (1888) Zur lehre von der wirkung der slaze. *Arch Exp Pathol Pharmakol (Leipzig)* 24:247–260.
2. Collins KD, Washabaugh MW (1985) The Hofmeister effect and the behaviour of water at interfaces. *Q Rev Biophys* 18:323–422.
3. Lo Nostro P, Ninham BW (2012) Hofmeister phenomena: An update on ion specificity in biology. *Chem Rev* 112:2286–2322.
4. Marcus Y (2009) Effect of ions on the structure of water: Structure making and breaking. *Chem Rev* 109:1346–1370.
5. Omta AW, Kropman MF, Woutersen S, Bakker HJ (2003) Negligible effect of ions on the hydrogen-bond structure in liquid water. *Science* 301:347–349.
6. Smith JD, Saykally RJ, Geissler PL (2007) The effects of dissolved halide anions on hydrogen bonding in liquid water. *J Am Chem Soc* 129:13847–13856.
7. Tobias DJ, Hemminger JC (2008) Chemistry. Getting specific about specific ion effects. *Science* 319:1197–1198.
8. Corridoni T, Mancinelli R, Ricci MA, Bruni F (2011) Viscosity of aqueous solutions and local microscopic structure. *J Phys Chem B* 115:14008–14013.
9. Funkner S, et al. (2012) Watching the low-frequency motions in aqueous salt solutions: The terahertz vibrational signatures of hydrated ions. *J Am Chem Soc* 134:1030–1035.
10. Vrbka L, Jungwirth P, Bauduin P, Touraud D, Kunz W (2006) Specific ion effects at protein surfaces: A molecular dynamics study of bovine pancreatic trypsin inhibitor and horseradish peroxidase in selected salt solutions. *J Phys Chem B* 110:7036–7043.
11. Zangi R, Hagen M, Berne BJ (2007) Effect of ions on the hydrophobic interaction between two plates. *J Am Chem Soc* 129:4678–4686.
12. Pegram LM, Record MT, Jr (2008) Thermodynamic origin of Hofmeister ion effects. *J Phys Chem B* 112:9428–9436.
13. Zhang Y, Cremer PS (2010) Chemistry of Hofmeister anions and osmolytes. *Annu Rev Phys Chem* 61:63–83.
14. Jungwirth P, Tobias DJ (2006) Specific ion effects at the air/water interface. *Chem Rev* 106:1259–1281.
15. Pegram LM, Record MT, Jr (2006) Partitioning of atmospherically relevant ions between bulk water and the water/vapor interface. *Proc Natl Acad Sci USA* 103:14278–14281.
16. Pegram LM, Record MT, Jr (2007) Hofmeister salt effects on surface tension arise from partitioning of anions and cations between bulk water and the air-water interface. *J Phys Chem B* 111:5411–5417.
17. Chang TM, Dang LX (2006) Recent advances in molecular simulations of ion solvation at liquid interfaces. *Chem Rev* 106:1305–1322.
18. Liu D, Ma G, Levering LM, Allen HC (2004) Vibrational spectroscopy of aqueous sodium halide solutions and air-liquid interfaces: Observation of increased interfacial depth. *J Phys Chem B* 108:2252–2260.
19. Ghosal S, et al. (2005) Electron spectroscopy of aqueous solution interfaces reveals surface enhancement of halides. *Science* 307:563–566.
20. Petersen PB, Saykally RJ (2006) On the nature of ions at the liquid water surface. *Annu Rev Phys Chem* 57:333–364.
21. Brown MA, et al. (2008) Ion spatial distributions at the liquid-vapor interface of aqueous potassium fluoride solutions. *Phys Chem Chem Phys* 10:4778–4784.
22. Tian C, Byrnes SJ, Han H-L, Shen YR (2011) Surface propensities of atmospherically relevant ions in salt solutions revealed by phase-sensitive sum frequency vibrational spectroscopy. *J Phys Chem Lett* 2:1946–1949.
23. Gopalakrishnan S, Jungwirth P, Tobias DJ, Allen HC (2005) Air-liquid interfaces of aqueous solutions containing ammonium and sulfate: Spectroscopic and molecular dynamics studies. *J Phys Chem B* 109:8861–8872.
24. Jungwirth P, Tobias DJ (2001) Molecular structure of salt solutions: A new view of the interface with implications for heterogeneous atmospheric chemistry. *J Phys Chem B* 105:10468–10472.
25. Jungwirth P, Tobias DJ (2002) Ions at the air/water interface. *J Phys Chem B* 106: 6361–6373.
26. Randalls JEB (1977) Structure at the free surface of water and aqueous electrolyte solutions. *Phys Chem Liquids* 7:107–179.
27. Hua W, Verreault D, Huang Z, Adams EM, Allen HC (2014) Cation effects on interfacial water organization of aqueous chloride solutions. I. Monovalent cations: Li^+, Na^+, K^+, and NH_4^+. *J Phys Chem B* 118:8433–8440.
28. Hua W, Verreault D, Allen HC (2014) Surface electric fields of aqueous solutions of NH_4NO_3, $Ng(NO_3)_2$, $NaNO_3$, and $LiNO_3$: Implications for atmospheric aerosol chemistry. *J Phys Chem C* 118:24941–24949.
29. Ottosson N, Faubel M, Bradforth SE, Jungwirth P, Winter B (2010) Photoelectron spectroscopy of liquid water and aqueous solution: Electron effective attenuation lengths and emission-angle anisotropy. *J Electron Spectros Relat Phenomena* 177:60–70.
30. Ottosson N, et al. (2010) The influence of concentration on the molecular surface structure of simple and mixed aqueous electrolytes. *Phys Chem Chem Phys* 12:10693–10700.
31. Cheng MH, et al. (2012) Ambient pressure X-ray photoelectron spectroscopy and molecular dynamics simulation studies of liquid/vapor interfaces of aqueous NaCl, RbCl, and RbBr solutions. *J Phys Chem C* 116:4645–4655.
32. Tissot H, et al. (2015) Cation depth-distribution at alkali halide aqueous solution surfaces. *J Phys Chem C* 119:9253–9259.
33. Weissenborn PK, Pugh RJ (1996) Surface tension of aqueous solutions of electrolytes: Relationship with ion hydration, oxygen solubility, and bubble coalescence. *J Colloid Interface Sci* 184:550–563.
34. Horinek D, et al. (2009) Specific ion adsorption at the air/water interface: The role of hydrophobic solvation. *Chem Phys Lett* 479:173–183.
35. Bresme F, Chacón E, Tarazona P, Wynveen A (2012) The structure of ionic aqueous solutions at interfaces: An intrinsic structure analysis. *J Chem Phys* 137:114706.
36. Hahn C, Kann ZR, Faust JA, Skinner JL, Nathanson GM (2016) Super-Maxwellian helium evaporation from pure and salty water. *J Chem Phys* 144:044707.
37. Yeh JJ, Lindau I (1985) Atomic subshell photoionization cross-section and asymmetry parameters–$1 \leq Z \leq 103$. *At Data Nucl Data Tables* 32:1–155.
38. Thürmer S, et al. (2013) Photoelectron angular distributions from liquid water: Effects of electron scattering. *Phys Rev Lett* 111:173005.
39. Olivieri G, Parry KM, Powell CJ, Tobias DJ, Brown MA (2016) Quantitative interpretation of molecular dynamics simulations for X-ray photoelectron spectroscopy of aqueous solutions. *J Chem Phys* 144:154704.
40. Marcus Y (1988) Ionic radii in aqueous solutions. *Chem Rev* 88:1475–1498.
41. Willard AP, Chandler D (2010) Instantaneous liquid interfaces. *J Phys Chem B* 114: 1954–1958.
42. Stern AC, Baer MD, Mundy CJ, Tobias DJ (2013) Thermodynamics of iodide adsorption at the instantaneous air-water interface. *J Chem Phys* 138:114709.
43. Arslanargin A, Beck TL (2012) Free energy partitioning analysis of the driving forces that determine ion density profiles near the water liquid-vapor interface. *J Chem Phys* 136:104503.
44. Baer MD, Stern AC, Levin Y, Tobias DJ, Mundy CJ (2012) Electrochemical surface potential due to classical point charge models drives anion adsorption to the air-water interface. *J Phys Chem Lett* 3:1565–1570.
45. Otten DE, Shaffer PR, Geissler PL, Saykally RJ (2012) Elucidating the mechanism of selective ion adsorption to the liquid water surface. *Proc Natl Acad Sci USA* 109:701–705.
46. Ben-Amotz D (2016) Interfacial solvation thermodynamics. *J Phys Condens Matter* 28: 414013.
47. Tobias DJ, Stern AC, Baer MD, Levin Y, Mundy CJ (2013) Simulation and theory of ions at atmospherically relevant aqueous liquid-air interfaces. *Annu Rev Phys Chem* 64: 339–359.
48. Ogletree DF, et al. (2002) A differentially pumped electrostatic lens system for photoemission studies in the millibar range. *Rev Sci Instrum* 73:3872–3877.
49. Bluhm H, et al. (2006) Soft X-ray microscopy and spectroscopy at the molecular environmental science beamline at the advanced light source. *J Electron Spectros Relat Phenomena* 150:86–104.
50. Starr DE, Wong EK, Worsnop DR, Wilson KR, Bluhm H (2008) A combined droplet train and ambient pressure photoemission spectrometer for the investigation of liquid/vapor interfaces. *Phys Chem Chem Phys* 10:3093–3098.
51. Ogletree DF, Bluhm H, Hebenstreit ED, Salmeron M (2009) Photoelectron spectroscopy under ambient pressure and temperature conditions. *Nucl Instrum Methods Phys Res A* 601:151–160.
52. Bluhm H (2010) Photoelectron spectroscopy of surfaces under humid conditions. *J Electron Spectros Relat Phenomena* 177:71–84.
53. Henke BL, Gullikson EM, Davis JC (1993) X-ray interactions–Photoabsorption, scattering, transmission, and reflection at E=50-30,000 eV, Z=1-92. *At Data Nucl Data Tables* 54:181–342.
54. Berendsen HJC, Grigera JR, Straatsma TP (1987) The missing term in effective pair potentials. *J Phys Chem* 91:6269–6271.
55. Van Der Spoel D, et al. (2005) GROMACS: Fast, flexible, and free. *J Comput Chem* 26: 1701–1718.
56. Berendsen HJC, Postma JPM, van Gunsteren WF, DiNola A, Haak JR (1984) Molecular-dynamics with coupling to an external bath. *J Chem Phys* 81:3684–3690.
57. Bussi G, Donadio D, Parrinello M (2007) Canonical sampling through velocity rescaling. *J Chem Phys* 126:014101.
58. Miyamoto S, Kollman PA (1992) An analytical version of the shake and rattle algorithm for rigid water models. *J Comput Chem* 13:952–962.
59. Essmann U, et al. (1995) A smooth particle mesh Ewald method. *J Chem Phys* 103: 8577–8593.